Minimum Variance Imaging in Plates Using Guided Wave Mode Beamforming

Simone Sternini, Annamaria Pau, and Francesco Lanza di Scalea, *Senior Member, IEEE*

***Abstract*—This paper presents improvements to ultrasonic imaging of solid plate-like structures using the minimum variance distortionless response (MVDR) beamforming processor. The primary application of this work is the nondestructive testing of plate-like components that are widely used in aerospace, marine, and civil structures. The study proposes a new set of weights, or MVDR replica vectors, that are based on the physics of the propagating Lamb modes, including the symmetric mode S0, the antisymmetric mode A0, and the shear horizontal mode SH0. Numerical results show that these wave mode weights, combined with geometrical spreading, improve the focus of the array by increasing dynamic range and spatial resolution of the image. Additionally, quite dramatic improvements in image quality are achieved by combining, or compounding, the multiple Lamb modes naturally present in the plate in both transmission and reflection. As shown in recent work applied to bulk waves in 3D solids, the compounding of Lamb modes in plates increases the array gain without increasing its physical aperture.**

***Index Terms*—Ultrasonic imaging, guided waves, matched field processing (MFP), minimum variance distortionless response (MVDR), wave structure, image compounding, nondestructive testing (NDT).**

I. Introduction

ULTRASONIC imaging is utilized in a wide range of applications from the medical field to the inspection of structural components. Continued research in this area has allowed ultrafast cardiac imaging [1]-[4] and blood flow imaging [5]-[11], as well as effective nondestructive testing (NDT) of structures for damage detection and characterization [12]-[29].

Most of the ultrasonic imaging beamformers involve the use of weighting functions, often called apodization weights, attributed to the collected waveforms to suppress the sidelobes in the final image. Usually, these apodization weights are static (e.g. Hanning window), therefore they do not change with respect to different focus points in the imaging medium. A different application of these weights can be found in a Matched Field Processing framework [30], [31], where they serve as a filtering tool to locate the reflector using the recorded signals. In this implementation, weights are often referred to as "replica vectors" since they "replicate" the expected response of the array for a specific recorded feature. The overall concept is to find the best match between the replica vectors, calculated for each discretized point in the imaging medium, and the "data vector" measured by the transducer array. The points showing the best match are the true locations of the reflectors. A common set of weights (replicas) accounts for the geometrical spreading of the waves travelling through the material, which involves an amplitude decay proportional to $1/\sqrt{d}$ for the 2D case and $1/d$ for the 3D case, where d is the propagation distance [18], [19], [23]. Other types of weights, instead, account for the scattering patterns of the wave reflected by a given structural feature [23], [24].

A known beamforming algorithm found in matched field processing is the minimum variance distortionless response (MVDR) method. MVDR, also known as Capon's Maximum Likelihood Method (MLM), has been around since the 1960s [32] and has found numerous applications in underwater acoustics, structural damage detection [18], [19], [24] and, more recently, medical imaging [33]-[36]. The MVDR beamformer is an adaptive processor, which means that the weights depend both on the replica field (expected response) and on the actual measured data. This processor is able to suppress the sidelobe level while narrowing the main lobe in the beamformer pattern. The concept behind MVDR is to minimize the output of the array except in the "look direction", so as to reject any signal (or noise) coming from a direction different from the direction of scanning. The MVDR beamformer is strongly affected by the model used to describe the imaging medium, therefore an accurate representation of the wave propagation characteristics is a crucial part needed to create a reliable replica field.

A strategy used to increase the array gain without increasing its physical aperture is compounding. The idea is to combine images obtained with different independent parameters in order to increase the image contrast and spatial resolution. Examples of compounding can be found in matched field acoustics, where images from multiple frequencies are combined [37], or in medical imaging, in the form of plane wave compounding [1]. There are two main ways of compounding images (or features): incoherently [30], [37]-[39], or coherently [38], [40]-[42].

This work was supported by US Federal Railroad Administration contract no. DTFR5316C00024, by US National Science Foundation grant no. CMMI-1362144, and by Ateneo Sapienza and PRIN 2015.

S. Sternini and F. Lanza di Scalea are with the Experimental Mechanics & NDE Laboratory, Department of Structural Engineering, University of California at San Diego, La Jolla, CA 92093 USA (e-mail: sisternini@ucsd.edu and flanzadiscalea@ucsd.edu).

A. Pau is with the Department of Structural and Geotechnical Engineering, Sapienza University of Rome, via Gramsci 42, Rome, 00197 Italy.

While in theory the coherent version should bring additional gain due to the added cross terms, the relative performance generally depends on the noise structure in the imaging medium [38], [40]. The authors have recently demonstrated the benefits of compounding for the case of bulk waves in 3D solids [25], by combining images from longitudinal and shear waves naturally coexisting in the imaging medium.

This paper extends some of these ultrasonic imaging strategies based on matched field processing (MVDR) to the case of guided (Lamb) waves in plate-like solid components that are widely used in aerospace, marine, and civil structures. The direct application of this paper is the improvement of the visualization of defects in these structures, in terms of increased dynamic range and spatial resolution performances. Guided-wave ultrasonic testing has arguably become in recent years the most popular technique for structural health monitoring (SHM). In particular, the paper proposes new weight vectors (replica vectors) based on the physics of the propagating Lamb modes to increase the focus of the array on the reflector (e.g. damage) locations. The paper also exploits the compounding of multiple Lamb modes to improve the imaging results compared to the traditional use of a single Lamb mode. The improvements are shown in a proof-of-principle numerical test of an aluminum plate with a blind hole reflector located either on-axis or off-axis relative to the transducer array. The case of multiple reflectors on the plate has been also investigated.

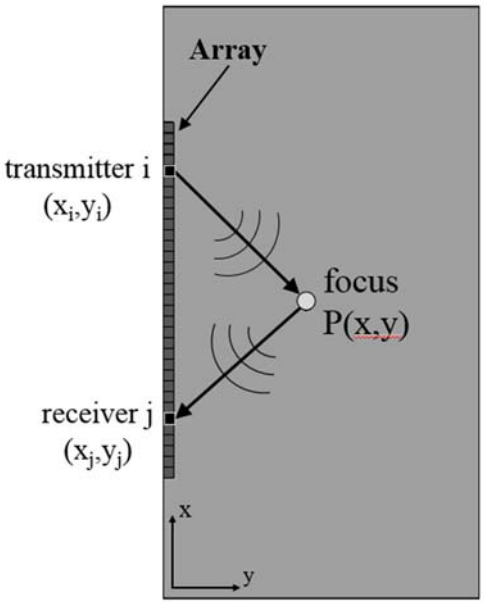

Fig. 1. Schematic of ultrasonic imaging on a plate.

II. Minimum Variance Distortionless Response Processor

Considering an array of M transmitters and N receivers (Fig. 1), let the spatial coordinates of each transmitter $i = 1..M$ be (x_i, y_i) and the spatial coordinates of each receiver $j = 1..N$ be (x_j, y_j). From the recorded waveforms, it is possible to extract amplitudes A from the time domain signals based on the travel time of a specific guided wave mode from transmitter i to focus point $P(x,y)$, and back to receiver j. For each focus point $P(x,y)$ and each transmitter i, a vector of amplitudes (data vector) can be constructed as follows

$$\overline{A_{i,xy}} = [\, A_{i1} \quad A_{i2} \quad \dots \quad A_{iN} \,]^T \tag{1}$$

where the superscript T denotes transpose and A_{ij} is the amplitude related to each transmitter-receiver pair i-j. The data vectors are then compared with the replica field, formed by the vectors of expected responses of the array, by means of the MVDR processor. Each focus point in the discretized imaging domain represents a "scanning" location where the data vector is compared with a replica vector. Hence the coordinates (x,y) of the focus points are used as parameters for which each replica field is constructed. Through this comparison, an ambiguity function is obtained, representing a map of similarity between data and replica vectors, which can be used to identify the reflectors (e.g. damage) anywhere in the plate. A high level of match, or similarity, between data and replicas will result in large intensity values in the ambiguity function, hence a "true" reflector.

The MVDR beamformer tries to optimize the match to a signal from a specific "look direction" while rejecting signals and correlated noise coming from different scanning locations. This procedure can be carried out by computing a replica vector $\overline{w_{ij,xy}^{MVDR}}$ that minimizes the output of the beamformer except in the "look direction" of scanning. The MVDR replica vector is chosen to minimize the following functional

$$F = \overline{w_{ij,xy}^{MVDR}}^T \overline{\overline{K_{xy}}}\, \overline{w_{ij,xy}^{MVDR}} + \gamma \left(\overline{w_{ij,xy}^{MVDR}}^T \overline{e_{ij,xy}} - 1 \right) \tag{2}$$

where γ is a Lagrange multiplier, and $\overline{e_{j,xy}}$ represents the normalized weighting functions (normalized replica vectors) on which the data vectors, forming the autocorrelation matrix $\overline{\overline{K_{xy}}}$, are projected. The matrix $\overline{\overline{K_{xy}}}$ is calculated as follows

$$\overline{\overline{K_{xy}}} = \frac{1}{M} \sum_{i=1}^{M} \overline{A_{i,xy}}\, \overline{A_{i,xy}}^T \tag{3}$$

where it is shown that the autocorrelation matrix for the focus point of coordinates (x,y) is calculated by the outer product of the data vectors computed in (1), averaged over M transmissions. Typically, the number of transmissions should be greater than or equal to the number of receivers for the autocorrelation matrix to have full rank. The normalized replica vectors are obtained as follows

$$\overline{e_{ij,xy}} = \frac{\overline{w_{ij,xy}}}{\left| \overline{w_{ij,xy}} \right|} \tag{4}$$

This article has been accepted for publication in a future issue of this journal, but has not been fully edited. Content may change prior to final publication. Citation information: DOI 10.1109/TUFFC.2019.2935139, IEEE Transactions on Ultrasonics, Ferroelectrics, and Frequency Control

so that the replica vectors, normalized by their L_2 norm, all have unit length. Section III will show how these replica vectors, or weights, can be constructed based on the physics of the propagating wave modes.

Taking the gradient of (2) with respect to $\overline{w_{j,xy}^{MVDR}}$ and setting it equal to zero results in

$$\overline{w_{ij,xy}^{MVDR}} = -\frac{\gamma}{2}\left(\overline{\overline{K_{xy}}}^{-1}\overline{e_{ij,xy}}\right) \tag{5}$$

and using the constraint condition of unity

$$\overline{w_{ij,xy}^{MVDR}}^{T}\overline{e_{ij,xy}} = 1 \tag{6}$$

it is possible to obtain the following expression for γ

$$\gamma = -2\left(\overline{e_{ij,xy}}^{T}\overline{\overline{K_{xy}}}^{-1}\overline{e_{ij,xy}}\right)^{-1}. \tag{7}$$

By substituting (7) into (5), the MVDR replica vector is obtained as [30], [31], [43]

$$\overline{w_{ij,xy}^{MVDR}} = \frac{\overline{\overline{K_{xy}}}^{-1}\overline{e_{ij,xy}}}{\overline{e_{ij,xy}}^{T}\overline{\overline{K_{xy}}}^{-1}\overline{e_{ij,xy}}} \tag{8}$$

which can be used in the MVDR beamformer as

$$B_{MVDR}(x,y) = \overline{w_{ij,xy}^{MVDR}}^{T}\overline{\overline{K_{xy}}}\,\overline{w_{ij,xy}^{MVDR}} \tag{9}$$

leading to the following final expression

$$B_{MVDR}(x,y) = \left[\overline{e_{ij,xy}}^{T}\overline{\overline{K_{xy}}}^{-1}\overline{e_{ij,xy}}\right]^{-1}. \tag{10}$$

Equation (8) shows that the weight vectors for the MVDR beamformer are constructed depending on the data itself. For this reason, MVDR is an *adaptive* beamforming technique and a nonlinear function of the received wave field. Equation (10) produces an ambiguity function, in the *(x,y)* location space, used for localizing the true reflectors.

Although MVDR has high resolution capabilities, modeling of the environment (replica field) should be carefully carried out. In fact, errors in the replica field deriving from geometrical or physical inaccuracies (e.g. transducer locations, wave mode velocities, etc.) can strongly affect the output of the MVDR beamformer and, in general, adaptive processes. Furthermore, as previously discussed, an insufficient number of transmissions could cause the autocorrelation matrix to be rank deficient [30]. In this case, the inverse of the autocorrelation matrix in (10) would not exist and a pseudoinverse matrix is required. To address these problems, a regularization procedure is performed using diagonal loading [18] of the autocorrelation matrix $\overline{\overline{K_{xy}}}$. A fraction *f* of the largest eigenvalue λ_1 of $\overline{\overline{K_{xy}}}$ is used for diagonal loading

$$\overline{\overline{K_{xy}}}^{-1} = \left(\overline{\overline{K_{xy}}} + f\lambda_1\overline{\overline{I}}\right)^{-1}. \tag{11}$$

For the MVDR results presented in this paper, the regularization factor *f* was chosen equal to 10^{-2}.

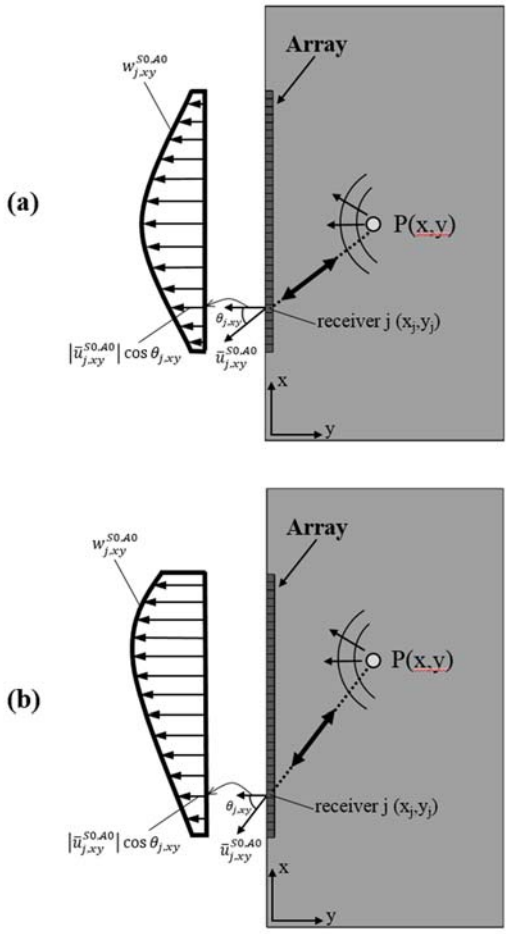

Fig. 2. Weight vectors, or replica vectors, based on wave mode structure for an S0 or A0 mode reflection. (a) Reflector located on-axis at the center of the array. (b) Reflector located off-axis.

III. Wave Mode Structure Weights

This work considers the three fundamental Lamb modes that can generally co-exist in a plate: symmetric (axial) mode S0, antisymmetric (flexural) mode A0, and shear horizontal mode SH0. The excitation frequency and thickness of the plate considered here were below the cutoff values for the higher-order modes, that were therefore ignored.

This article has been accepted for publication in a future issue of this journal, but has not been fully edited. Content may change prior to final publication. Citation information: DOI 10.1109/TUFFC.2019.2935139, IEEE Transactions on Ultrasonics, Ferroelectrics, and Frequency Control

Each wave mode that is reflected by a particular focus point will result in a particular distribution of responses across the array that can be used as the replica vector for the MVDR beamformer. In other words, the displacement "structure" of each mode can be used to generate the replica field.

A. S0 and A0 Wave Modes

For the case of an S0 or A0 wave mode reflected by point *P(x,y)* and impinging on receiver *j*, as illustrated in Fig. 2, the component of displacement considered for the replica vectors calculation is the displacement parallel to the wave propagation direction. Assuming that the array elements are only sensitive to the component of displacement along the normal to the surface (direction *y* in Fig. 1), it is possible to calculate the expected distribution of displacements across the array by simply projecting the wave vector $u_{j,xy}^{S0,A0}$ onto the *y* direction. This expected response of the array becomes the replica vector, or weight vector, for that particular reflector location *(x,y)*. By computing the expected array response for all possible reflector locations in the plate, a replica field can be constructed as follows

$$w_{j,xy}^{S0,A0} = \left|\overline{u_{j,xy}^{S0,A0}}\right| \cos\theta_{j,xy} = \left|\overline{u_{j,xy}^{S0,A0}}\right| \frac{\left|y_j - y\right|}{\sqrt{\left(x_j - x\right)^2 + \left(y_j - y\right)^2}} \quad (12)$$

or

$$w_{j,xy}^{S0,A0} \propto \frac{\left|y_j - y\right|}{\sqrt{\left(x_j - x\right)^2 + \left(y_j - y\right)^2}} \quad (13)$$

where the superscript *S0, A0* indicates a reflected S0 or A0 mode. Fig. 2(a) shows the response of the array for a reflector located on-axis at the center of the array. If the reflector is located off-axis, the distribution of amplitudes will be appropriately skewed, as shown in Fig. 2(b).

The geometrical spreading effect [18], [19], which also depends on the transmitter *i*, can be included in the calculation of the weights by modifying eq. (13) as follows

$$w_{ij,xy}^{S0,A0} \propto \frac{1}{\sqrt{d_{i,xy} d_{j,xy}}} \cdot \frac{\left|y_j - y\right|}{\sqrt{\left(x_j - x\right)^2 + \left(y_j - y\right)^2}} \quad (14)$$

where $d_{i,xy}$ is the distance between transmitter *i* and focus point *P(x,y)*, and similarly $d_{j,xy}$ is the distance between receiver *j* and the same focus point at *(x,y)*. Notice that the 2D geometrical spreading has been considered (square root of propagation distance). Equation (14) is the final relation for the calculation of wave mode weights for a reflected S0 or A0 mode (applicable to any wave mode used in transmission), and it depends on transmitter, receiver, and focus point location.

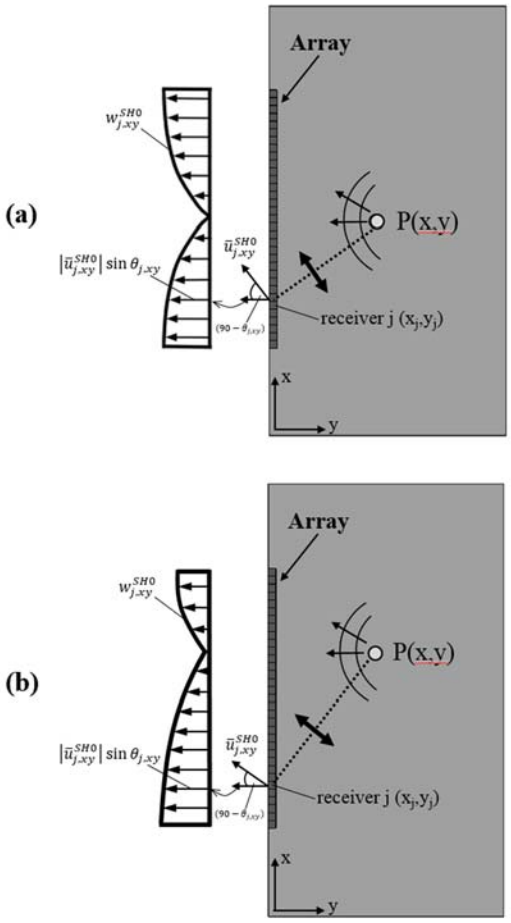

Fig. 3. Weight vectors, or replica vectors, based on wave mode structure for an SH0 mode reflection. (a) Reflector located on-axis at the center of the array. (b) Reflector located off-axis.

B. SH0 Wave Mode

The case of a shear horizontal (SH0) wave reflected by a focus point in the plate can be derived analogously. Fig. 3 illustrates the array response to an SH0 wave mode. In this case, the point motion is perpendicular to the wave propagation direction, similarly to shear waves in bulk solids. Since the array is still only sensitive to the displacement component along the normal to the surface (*y* direction), the SH0 displacement can be projected as in (12), thus giving the relation for SH0 wave mode weights as follows

$$w_{j,xy}^{SH0} = \left|\overline{u_{j,xy}^{SH0}}\right| \cos(90° - \theta_{j,xy}) = \left|\overline{u_{j,xy}^{SH0}}\right| \frac{\left|x_j - x\right|}{\sqrt{\left(x_j - x\right)^2 + \left(y_j - y\right)^2}} \quad (15)$$

Fig. 3(a) shows the array response for a reflector located on-axis to the array, and Fig. 3(b) shows the skewed response for a reflector located off-axis. By including 2D geometrical spreading, (15) becomes

This article has been accepted for publication in a future issue of this journal, but has not been fully edited. Content may change prior to final publication. Citation information: DOI 10.1109/TUFFC.2019.2935139, IEEE Transactions on Ultrasonics, Ferroelectrics, and Frequency Control

$$w_{ij,xy}^{SH0} \propto \frac{1}{\sqrt{d_{i,xy} d_{j,xy}}} \cdot \frac{|x_j - x|}{\sqrt{(x_j - x)^2 + (y_j - y)^2}} \quad (16)$$

Equation (16) is the final expression for wave mode weights applied to an SH0 wave reflection (applicable to any mode used in transmission).

IV. Guided Wave Mode Compounding

The multi-modal nature of Lamb waves (and guided waves in general) allows exploiting the different propagating modes to create multiple replica fields. If the information from the different modes can be combined, or compounded, very significant improvements in array gain can be obtained without increasing the array's physical aperture.

More specifically, in analogy to the case of bulk wave propagation in 3D solids examined recently by the authors [25], a reflector in a plate-like structure that is illuminated by a given incident Lamb mode can generate both same-mode reflections and mode-converted reflections. The results shown here consider both S0 transmissions and SH0 transmissions that can be generated simultaneously by a point-source acting in the mid-plane of the plate (see Fig. 4). The incident S0 mode can be reflected as a same-mode S0 ("S0-S0 combination") and a converted mode A0 ("S0-A0 combination"), if the reflector is generally not symmetric with respect to the mid-plane of the plate [44]. Also, the incident S0 can be generally mode-converted into a reflected SH0 mode ("S0-SH0 combination").

The test case considered in the paper consist of a blind hole in the plate as the reflector (simulating pitting corrosion) and allowing the following four mode combinations: S0-S0, S0-A0, S0-SH0, and SH0-SH0. Fig. 4 illustrates how the different transmitted modes (S0 and SH0) are reflected through either same-mode reflection or mode conversion. The dashed lines in Fig. 4 represent the main directivity lobes of the transmitted modes, whereas the solid lines indicate the directivity lobes of the reflected modes.

Wave mode compounding can be performed either incoherently or coherently. Incoherent compounding is the simple summation of the image intensities obtained by the different wave mode combinations. It is implemented as follows

$$B_{TOT,incoherent}(x,y) = \sum_{MC} B_{MVDR}^{MC}(x,y) \quad (17)$$

where *MC = S0-S0, S0-A0, S0-SH0, SH0-SH0* indicates the various wave mode combinations, and $B_{MVDR}^{MC}(x,y)$ (in decibels) is the image obtained using the MVDR algorithm for a specific mode combination. This incoherent approach exploits the consistency of the true reflector throughout the different mode combinations, while reducing the random spatial noise in each individual image.

Coherent compounding, instead, considers "cross-mode" terms that represent the spatial cross-correlation between the various images. The coherent way of combining different images comes from the "cross-frequency" terms used in matched field processing, which exploit the phase coherence of waves at different frequencies. In the coherent case, the final image intensity is

$$B_{TOT,coherent}(x,y) = \left(\sum_{MC} \left| \sqrt{B_{MVDR}^{MC}(x,y)} \right| \right)^2 \quad (18)$$

where, as in the incoherent case, the images $B_{MVDR}^{MC}(x,y)$ (in decibels) are given by (10) for the different wave mode combinations *MC*.

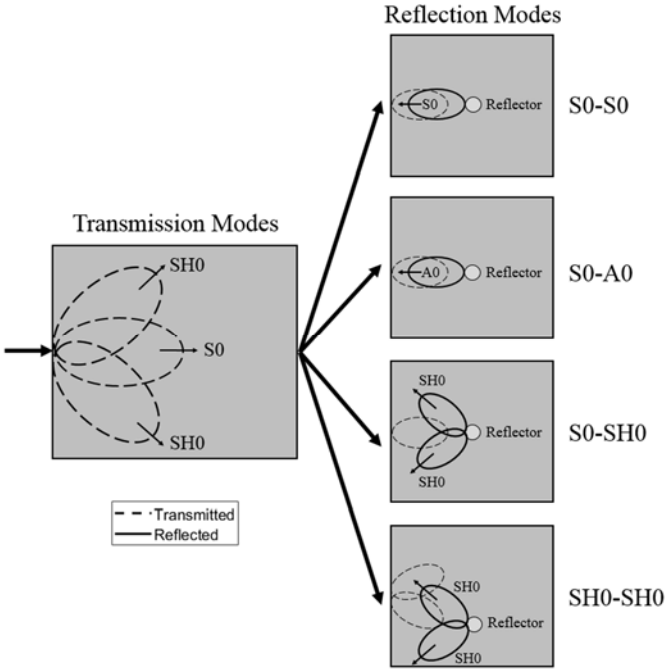

Fig. 4. Schematic of transmitted and reflected wave modes in a plate subjected to a point source parallel to the plane of the plate. The reflector is an antisymmetric defect (blind hole).

V. Numerical Results

A finite element model was created to simulate the propagation of guided Lamb waves in an aluminum plate with a blind hole as the reflector (simulating pitting corrosion). An on-axis hole and an off-axis hole were considered.

The transmission and reception of the guided waves was performed using a simulated 33-element linear array. The excitation considered to obtain the incident S0 and SH0 modes was a force parallel to the plane of the plate along direction *x*, applied as a point source (Fig. 4). All numerical waveforms were corrupted by adding artificial noise at a level of 30% of the waveform's Root Mean Square prior to applying the imaging algorithms. The following section presents the details of the model.

A. Finite Element Model

The Finite Element model (Fig. 5) describes a plate 0.45m x 0.76m in size and 9 mm in thickness. The material is aluminum

This article has been accepted for publication in a future issue of this journal, but has not been fully edited. Content may change prior to final publication. Citation information: DOI 10.1109/TUFFC.2019.2935139, IEEE Transactions on Ultrasonics, Ferroelectrics, and Frequency Control

with density 2810 kg/m^3, Young's modulus 7*10^{10} N/m^2, and Poisson's ratio 0.32. The model was run with the software Ansys using SHELL 181 elements. This is a 3D shell element with four nodes and six degrees-of-freedom per node, that are translations of the plane of the plate according to the three Cartesian axes and rotations about them. The plane of the plate is in the *x*-*y* plane, and the *z* axis is orthogonal to the plane. The shell element supports layered composites, and this property can be exploited to model the blind hole discontinuity. This is defined as a circular area made of two layers, occupying respectively the volume under and above the symmetry plane. One of the two layers has the same material properties as the rest of the plate, the second one has zero density and stiffness, to represent the missing part. In such a way, we can model an asymmetric blind hole with a thickness equal to 50% of the plate's thickness. Within the range of frequencies, wavelength and defects size under study, the shell model is able to appropriately describe the scattered field. This was proved by an independent analysis carried out on a 3D brick (SOLID 185) model of the plate with three degrees of freedom per node. The displacement time-histories recorded on the surface of the plate for both the through-thickness hole and the blind hole at two different receiver positions were not significantly different (in amplitude, shape or arrival times) between the two models.. This indicates that evanescent higher order modes, should they be present , rapidly decay and do not influence the response measured by the transducers.

The plate is clamped on one side and has free boundaries on the other three edges. Waves are generated using an in-plane point force whose time history is a six-cycle sine enveloped by a Gaussian curve (toneburst), with center frequency of ~ 90 kHz. Defining the bandwidth of a signal as the frequency band whose power is greater than 50% of the maximum power, time history of the used forcing function has a bandwidth of 0.2 MHz*mm. This results into a value for the product of excitation frequency and plate thickness of ~ 0.8 MHz*mm (with a -6dB bandwidth of 0.2 MHz*mm) where only the fundamental zero-order modes S0, SH0, and A0 can exist [45]. Time and space discretizations are appropriately scaled accounting for the wave physics. The time step is 5.5*10^{-7} s, which is 1/20 of the period of the travelling waves, and the largest size of the elements in the mesh is 1 mm, which is around 1/25 of the smallest wavelength involved, associated to the A0 mode.

The ability of shell elements to describe the interaction of S0 and SH0 waves with a through-thickness hole was proved in [46], in a comparison between FE results and analytical solutions. Moreover, the shell element capability to capture the evanescent part of the defect scattering for the A0 mode is described in [47].

The components of displacements for modes S0 and SH0 are directly obtained from the in-plane displacements in the plane of the plate, that are assumed to be constant through the plate thickness, and therefore coincide with those at the surface of the plate. On the contrary, the components of displacement for mode A0 at the surface of the plate are indirectly obtained from the rotations about the *x* and *y* axes, by assuming a linear distribution of displacements through the plate thickness (low frequency approximation).

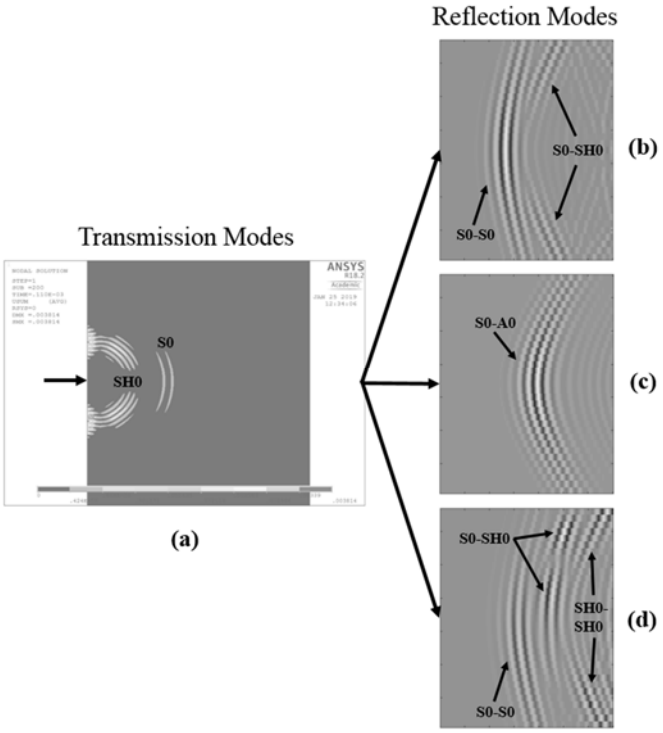

Fig. 5. Schematic of the Finite Element model used for the guided wave simulation on the aluminum plate. (a) S0 and SH0 transmission modes generated by a force parallel to the plane of the plate. (b) S0-S0 and S0-SH0 wave mode combinations reflected by the on-axis blind hole (b and c: center of the hole y = 0.38m). (c) S0-A0 combination reflected by the on-axis blind hole. (d) S0-S0, S0-SH0, and SH0-SH0 combinations reflected by the off-axis blind hole (d: center of the hole y = 0.30m).

The schematic of Fig. 4 is proved by the FE results reported in Fig. 5. Fig. 5(a) shows the contour plot of displacements at a given time instant, showing how the forcing function, applied at the plate centerline, generates both an S0 and SH0 wave. Figs. 5(b), (c), and (d) show the contour plot of the time-history of the displacement field recorded by the array of sensors for an on-axis defect with respect to the forcing function (Figs. (b) and (c)) and an off-axis defect (Fig. (d)). Figs. 5(b), (c), and (d) show how different guided waves are reflected by a blind hole reflector representing a non-symmetric defect with respect to the plane of the plate.

B. Results: Wave mode structure weights

The results compare the MVDR algorithm that uses geometrical spreading alone as the "look direction" (replica vectors) [18], [24], with one that uses replica vectors obtained from the proposed guided wave mode weights in (14) and (16) of Section III, which combine geometrical spreading with the wave mode structure. Fig. 6 shows the results obtained for the on-axis reflector. The aluminum plate dimensions were 0.45m in the *x* direction and 0.76m in the *y* direction. The blind hole was located at x = 0.19m and y = 0.38m, has a diameter of 20 mm, that is the same size of the smallest wavelength involved. The residual thickness of the plate at the blind hole is 45 mm. The results plot the power (in dB) of the beamformed acoustic

This article has been accepted for publication in a future issue of this journal, but has not been fully edited. Content may change prior to final publication. Citation information: DOI 10.1109/TUFFC.2019.2935139, IEEE Transactions on Ultrasonics, Ferroelectrics, and Frequency Control

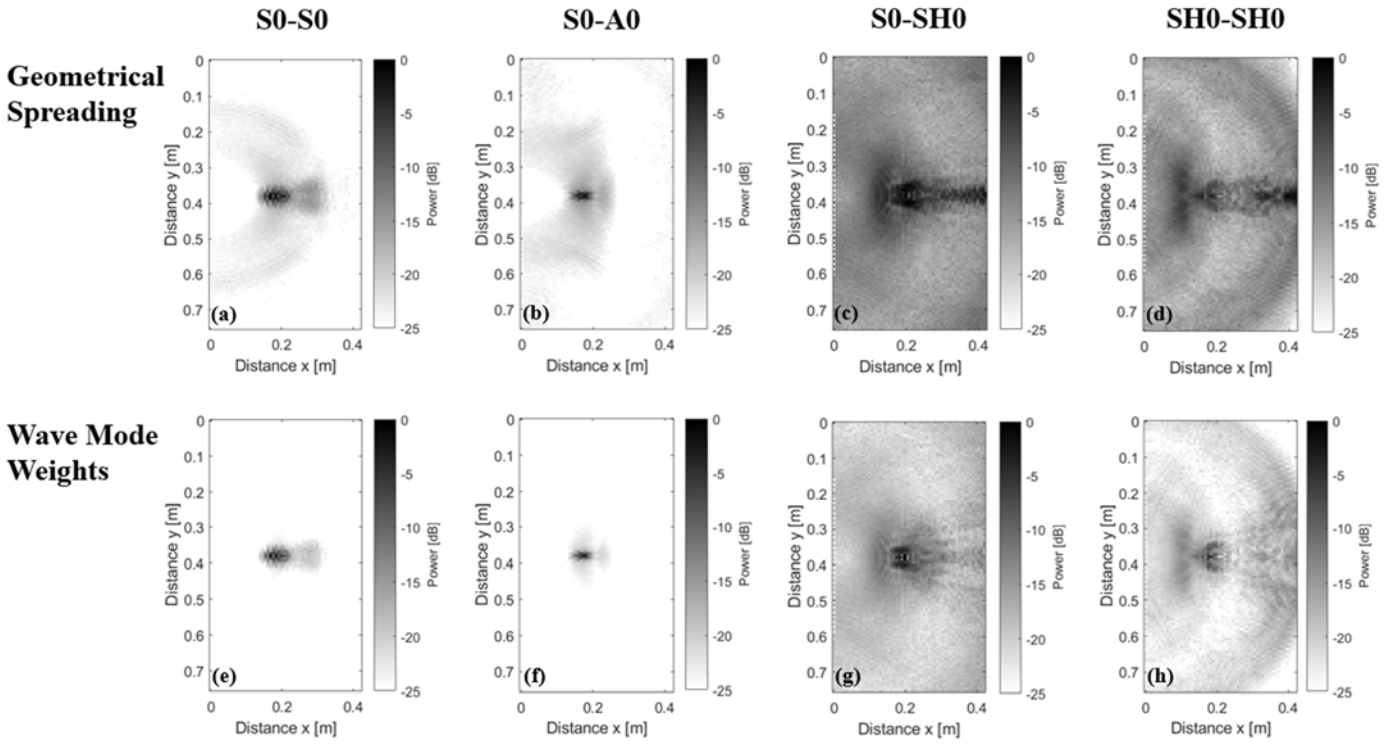

Fig. 6. Numerical results for the on-axis blind hole reflector obtained using MVDR with geometrical spreading only and with wave mode weights. (a)-(d) Results obtained with geometrical spreading for the S0-S0, S0-A0, S0-SH0, and SH0-SH0 combinations, respectively. (e)-(h) Results obtained using wave mode weights for the S0-S0, S0-A0, S0-SH0, and SH0-SH0 combinations, respectively. Coordinates of the defect center x=0.19, y=0.38 m.

feature recorded by the array, since the MVDR relation used to obtain the images, eq. (10), is a quadratic form. Baseline subtraction has been performed in order to remove reflections from the boundaries and cross-talk between the sensors in the array. Baseline waveforms were obtained from the same simulated plate with no blind hole defect. All images are plotted in the same dB scale (0 to -25dB) for a better comparison of the different sets of weights. Figs. 6(a)-6(d) are obtained using only geometrical spreading weights for the S0-S0, S0-A0, S0-SH0, and SH0-SH0 combinations, respectively. Figs. 6(e)-6(h) are obtained using the proposed wave mode structure weights for the same four combinations. Comparing Fig. 6(a) to Fig. 6(e), it is clear that the wave mode weights for the S0-S0 combinations considerably improve the imaging result. Specifically, the wave mode weights increase the dynamic range (lower noise floor) and suppress the sidelobes, compared to using only geometrical spreading weights. Similarly, for the S0-A0 combination (Figs. 6(b) and 6(f)), the dynamic range improves. Moreover, the S0-A0 combination achieves a higher spatial resolution compared to S0-S0 case, due to the smaller wavelength of the reflected A0 mode compared to the reflected S0 mode.

The third combination involves the mode conversion of S0 into SH0. Fig. 6(c) shows the result with the geometrical spreading weights. In this case, around the reflector location there are other high intensity areas which are likely artifacts deriving from other wave mode combinations. The reflection from the boundary on the right side of the plate also appears in the image. Fig. 6(g) illustrates the image obtained using the same S0-SH0 combination, with the application of the wave mode weights. In this case, the improvement from Fig. 6(c) is evident, as the artifacts and the reflection from the boundary are eliminated, and the energy is correctly focused on the true reflector. A slight improvement in dynamic range is also visible.

Finally, the last combination, SH0-SH0, is shown in Figs. 6(d) and 6(h). Similarly to the S0-SH0 combination, the geometrical spreading weights generate artifacts from other wave move combinations and boundary reflections on the right edge of the plate. The application of the wave mode weights considerably reduces both artifacts and reflections, and increases the dynamic range by lowering the noise floor of the image.

In general, the S0-S0 and S0-A0 combinations carry more energy than the S0-SH0 and SH0-SH0 combinations, as seen from the images of Fig. 6, thus resulting in a lower noise floor. This is partly due to the fact that more energy is transferred from the incident S0 mode into a reflected S0 mode, or into a mode converted A0 mode. Furthermore, given the normal point excitation force used in the simulations, the transmitted SH0 mode carry less energy than the transmitted S0 mode.

Fig. 7 shows the Line Spread Functions (LSFs) obtained from the images of Fig. 6 by plotting the intensity distribution along the y direction at x = 0.19m (reflector location). All four plots show an improvement in dynamic range when the wave mode weights are applied. Fig. 7(a) shows that the wave mode weights for the S0-S0 combination increase the dynamic range by about 5dB compared to the geometrical spreading only. Similarly, the S0-A0 combination (Fig. 7(b)) shows an average improvement of 3dB. The S0-SH0 case in Fig. 7(c) shows a similar increase in dynamic range, around 5dB, as in Fig. 7(a).

This article has been accepted for publication in a future issue of this journal, but has not been fully edited. Content may change prior to final publication. Citation information: DOI 10.1109/TUFFC.2019.2935139, IEEE Transactions on Ultrasonics, Ferroelectrics, and Frequency Control

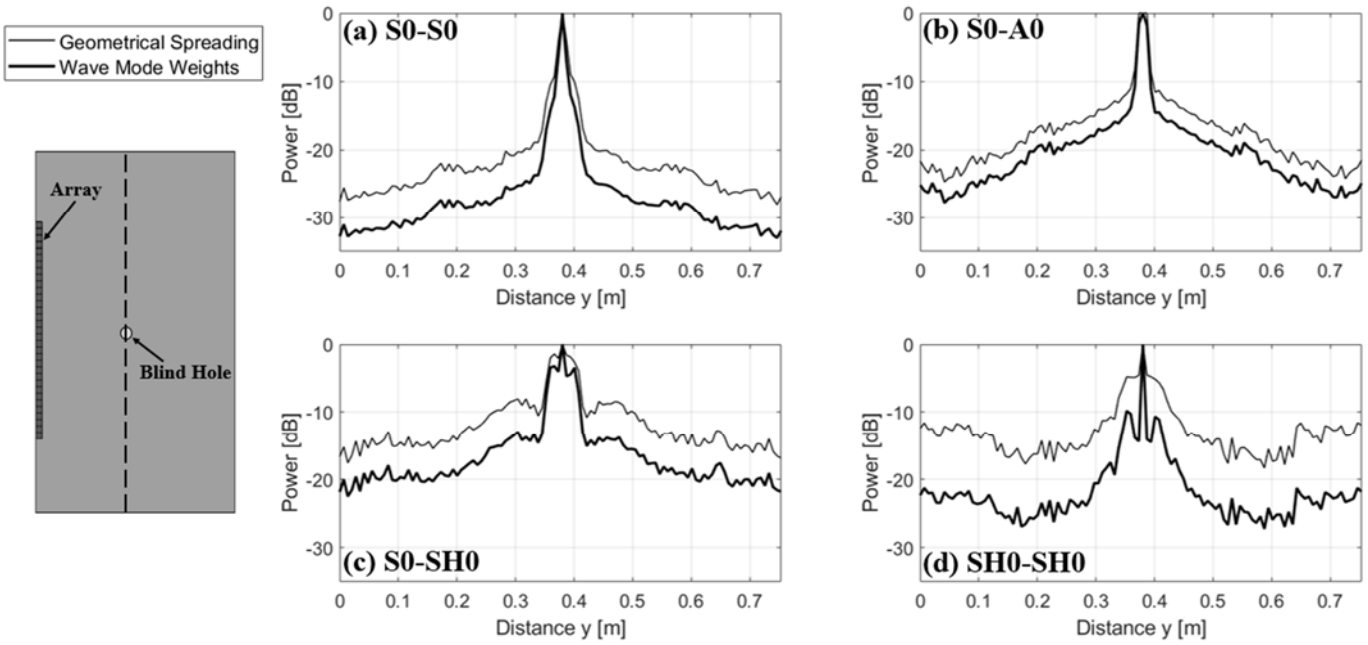

Fig. 7. Line Spread Functions (LSFs) along the *y* direction for the on-axis blind hole reflector for geometrical spreading only (thin solid line) and for the wave mode weights (thick solid line). (a) S0-S0 combination. (b) S0-A0 combination. (c) S0-SH0 combination. (d) SH0-SH0 combination. Coordinates of the defect center x=0.19, y=0.38 m.

The last combination, SH0-SH0, in Fig. 7(d) has the best of dynamic range improvement, lowering the noise floor by 10dB relative to the geometrical spreading case.

In terms of spatial resolution, the two sets of weights behave in a similar manner, with the largest improvements brought by the wave mode weights in the S0-SH0 and SH0-SH0 combinations. The metric used to compare the spatial resolution performance is the full width of the main lobe of the LSF at -6dB. For the S0-S0 combination, the width of the main lobe obtained with wave mode weights shows a decrease of about 6.80mm compared to the geometrical spreading case, thus showing an increase in spatial resolution. For the other wave modes, the width of the main lobe at -6dB decreased by 3.38mm, 8.54mm, and 57.05mm for the S0-A0, S0-SH0, and SH0-SH0 combinations, respectively, when the wave mode weights are applied.

These improvements in dynamic range and spatial resolution are expected since the wave mode weights applied to the

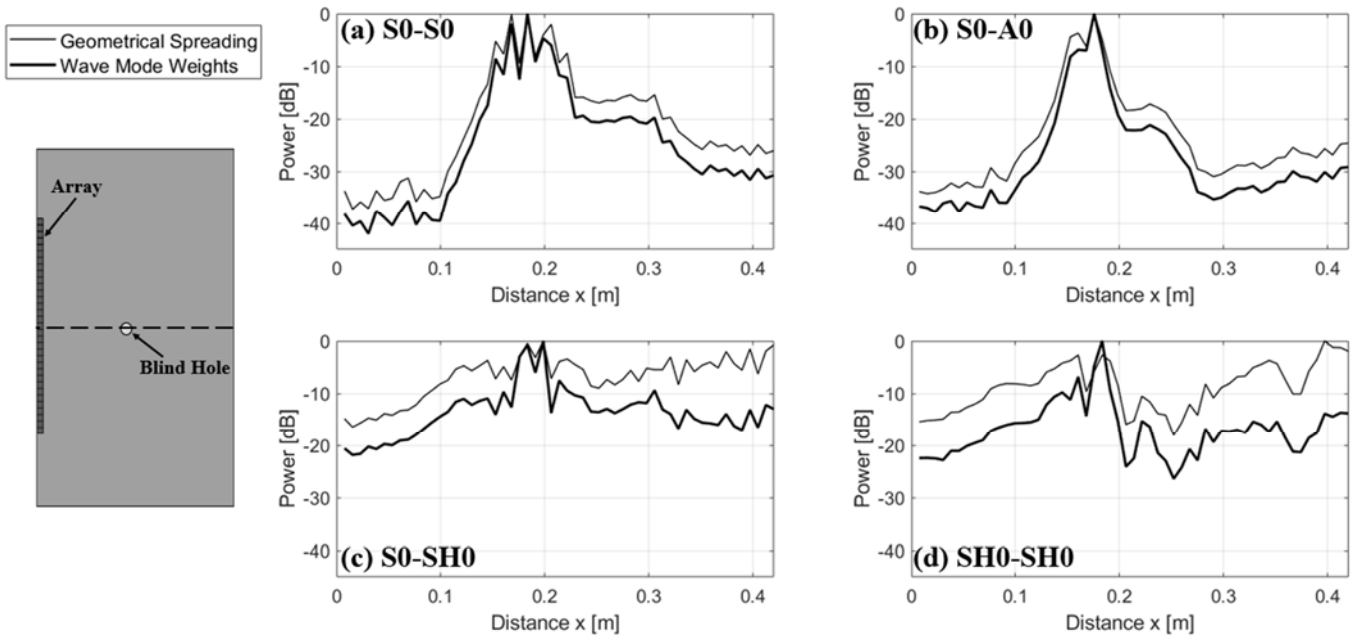

Fig. 8. Line Spread Functions (LSFs) along the *x* direction for the on-axis blind hole reflector for geometrical spreading only (thin solid line) and wave mode weights (thick solid line). (a) S0-S0 combination. (b) S0-A0 combination. (c) S0-SH0 combination. (d) SH0-SH0 combination. Coordinates of the defect center x=0.19, y=0.38 m.

This article has been accepted for publication in a future issue of this journal, but has not been fully edited. Content may change prior to final publication. Citation information: DOI 10.1109/TUFFC.2019.2935139, IEEE Transactions on Ultrasonics, Ferroelectrics, and Frequency Control

MVDR algorithm force the array to look for the best match between expected and recorded guided wave structures across the array. This requirement constitutes a much stronger constraint than the one imposed by the geometrical spreading weights alone.

Fig. 8 presents the LSFs results along the *x* direction, plotted at y = 0.38m (reflector location). This set of axial LSFs confirms how artifacts and boundary reflections can be suppressed using the wave mode weights. Overall, all four mode combinations show an increase in dynamic range when the wave mode weights are applied, compared to the geometrical spreading weights. Specifically, the S0-S0 and the S0-A0 combinations show an average increase in dynamic range of 4dB. The S0-SH0 combination has an increase in dynamic range of about 5dB, with local increases of up to 12dB close to the boundary. Similarly, the SH0-SH0 mode combination shows an average 8dB increase, reaching 13dB at the boundary. The axial resolution does not show a noticeable improvement, since this parameter is mainly influenced by the excitation frequency (or pulse width) of the transmitted signal, which is constant for both sets of weights.

The differences between the actual and the detected position of the defect along the x direction (axial position) were 0.022m, 0.022m, 0.0085m, and 0.0144m for the S0-S0, the S0-A0, the S0-SH0, and the SH0-SH0 combinations, respectively. Along the y direction (lateral position), all four mode combinations detected the defect at the correct location (y = 0.38m).

It is worth noticing how the wave mode weights help limit artifacts. Due to the different wave speeds of the three guided wave modes considered, "ghost" images of the reflector can be generated by a simple time backpropagation algorithm. Since the wave mode weights rely on the match between expected and measured wave structure across the array (which is different for every point in the imaging domain), there will be only a good match with the wave mode combination corresponding to a specific set of weights, while the other combinations will be "rejected" (poor match). For example, the values around x = 0.1m in Fig. 8(d) correspond to a "faster" combination than SH0-SH0 and using the wave mode weights it is possible to suppress it by ~ 8dB, so as to allow the correct identification of the true reflector. Furthermore, the S0-SH0 and the SH0-SH0 combinations show high intensity values close to the right boundary of the plate (for SH0-SH0 the boundary reflection has even a larger value of intensity compared to the reflector) when geometrical spreading weights are used. Applying the wave mode weights allows reducing the boundary reflection and focusing on the real location of the damage (Figs. 8(c) and 8(d)).

C. *Results: Wave mode compounding*

Fig. 9 shows the effect of compounding the four wave mode combinations for the on-axis reflector. The incoherent compounding is shown in Fig. 9(a) and the coherent compounding in Fig. 9(b). Comparing the images in Fig. 9 with the individual combinations in Fig. 6, it is clear that compounding brings a quite dramatic improvement to the image focus and gain. Fig. 9 also shows that the added cross-mode terms of the coherent compounding bring some additional improvements in image focus compared to the incoherent compounding.

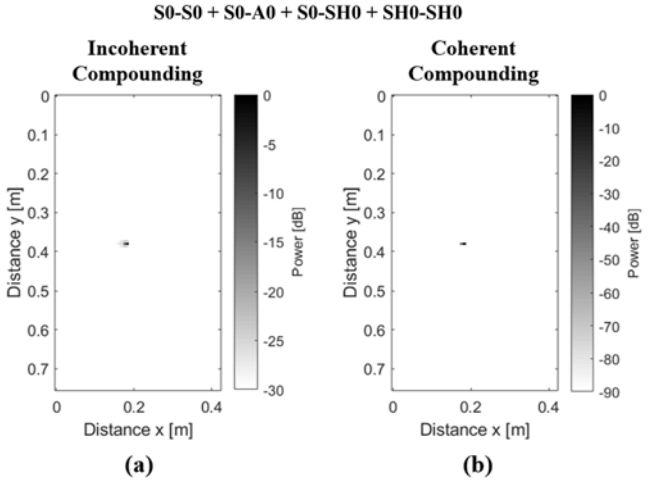

Fig. 9. Results obtained for the on-axis blind hole reflector after compounding the S0-S0, S0-A0, S0-SH0, and SH0-SH0 wave mode combinations (a) incoherently and (b) coherently. Coordinates of the defect center *x*=0.19, *y*=0.38 m.

The difference between the actual and the detected position of the defect was 0.0067m along the x direction (axial position) for both incoherent and coherent compounding. Along the y direction (lateral position) the detected location was equal to the real one (y = 0.38m).

D. *Results: Off-axis reflector*

The second proof-of-principle test was performed considering an off-axis blind hole reflector located at x = 0.19m and y = 0.30m. Fig. 10 shows the results with the wave mode weights compared to the geometrical spreading only for the four wave mode combinations. Analogously to Fig. 6, the wave mode weights show improvements with respect to the geometrical spreading weights in terms of dynamic range and spatial resolution. All images are plotted from 0dB to -25dB for ease of comparison with the on-axis case. In the S0-S0 combination in Figs. 10(a) and 10(e), the noise floor is lowered, and the sidelobes are suppressed when wave mode weights are applied. Similarly, in the S0-A0 combination, Figs. 10(b) and 10(f), a considerable increase in dynamic range is seen. Figs. 10(c) and 10(g) show the S0-SH0 case where, besides a slight increase in dynamic range, reflections from the boundaries and artifacts from other wave modes are reduced when wave mode weights are used. The SH0-SH0 combination shown in Figs. 10(d) and 10(h) shows similar improvements in reducing undesired artifacts and edge reflections.

The improvements in spatial resolution can be better appreciated by looking at the LSFs for the off-axis case. Fig. 11 shows the lateral LSFs plotted across the *y* direction at x = 0.19m (reflector location). The application of the wave mode weights reduces the main lobe of the LSFs, compared to geometrical spreading only, by 2.25mm, 5.65mm, 42.80mm, and 55.74mm for S0-S0, S0-A0, S0-SH0, and SH0-SH0,

This article has been accepted for publication in a future issue of this journal, but has not been fully edited. Content may change prior to final publication. Citation information: DOI 10.1109/TUFFC.2019.2935139, IEEE Transactions on Ultrasonics, Ferroelectrics, and Frequency Control

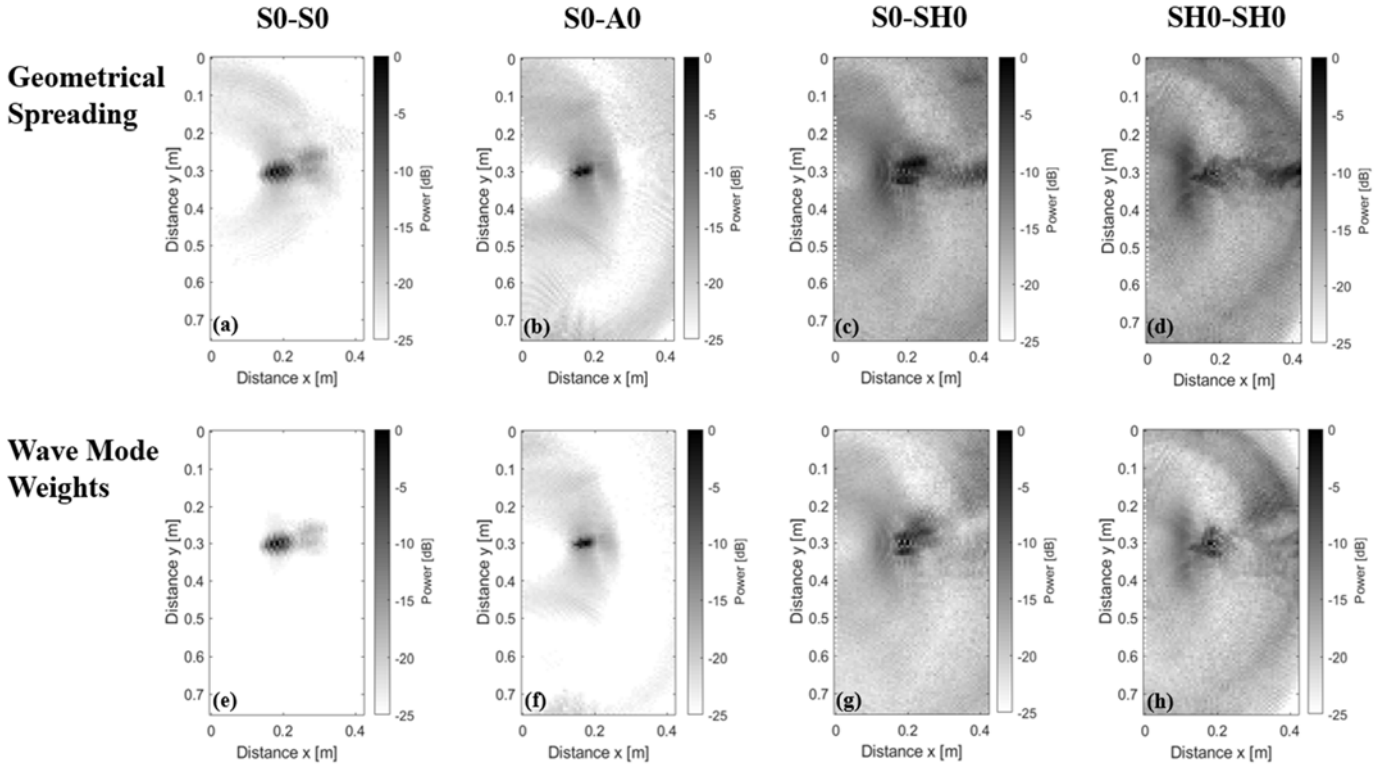

Fig. 10. Numerical results for the off-axis damage obtained using MVDR with geometrical spreading only and wave mode weights. (a)-(d) Results obtained with geometrical spreading for the S0-S0, S0-A0, S0-SH0, and SH0-SH0 combinations, respectively. (e)-(h) Results obtained using wave mode weights for the S0-S0, S0-A0, S0-SH0, and SH0-SH0 combinations, respectively. Coordinates of the defect center x=0.19, y=0.30 m.

respectively. Furthermore, the dynamic range shows an average increase of 5dB in the S0-S0, S0-SH0, and SH0-SH0 cases, and 3dB in the S0-A0 case.

The axial LSFs, plotted across the x direction and at y = 0.30m (reflector location), are shown in Fig. 12. Similarly to the on-axis case, all four combinations show that the two sets of weights present similar axial resolution performances. The dynamic range, instead, increases 4dB for S0-S0, 3dB for S0-A0, and from 5dB to 10dB for S0-SH0 and SH0-SH0, when wave mode weights are used. Figs. 12(c) and 12(d) show the

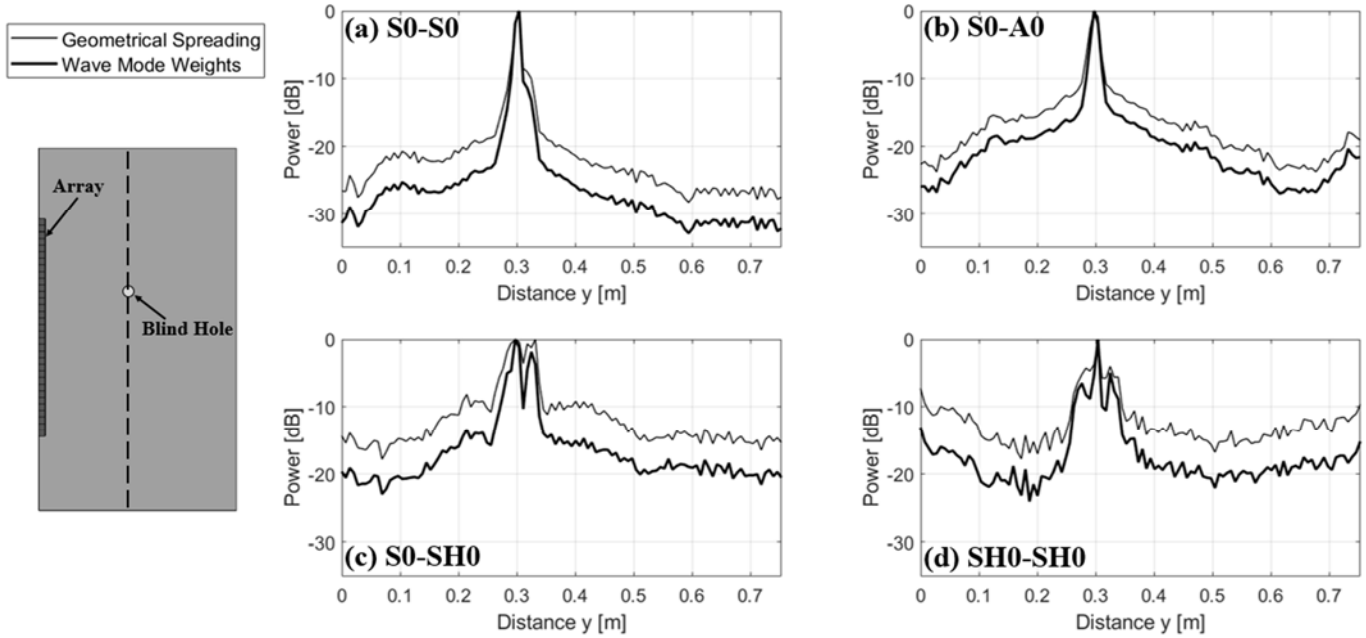

Fig. 11. Line Spread Functions (LSFs) along the y direction for the off-axis blind hole reflector for geometrical spreading only (thin solid line) and wave mode weights (thick solid line). (a) S0-S0 combination. (b) S0-A0 combination. (c) S0-SH0 combination. (d) SH0-SH0 combination. Coordinates of the defect center x=0.19, y=0.30 m.

This article has been accepted for publication in a future issue of this journal, but has not been fully edited. Content may change prior to final publication. Citation information: DOI 10.1109/TUFFC.2019.2935139, IEEE Transactions on Ultrasonics, Ferroelectrics, and Frequency Control

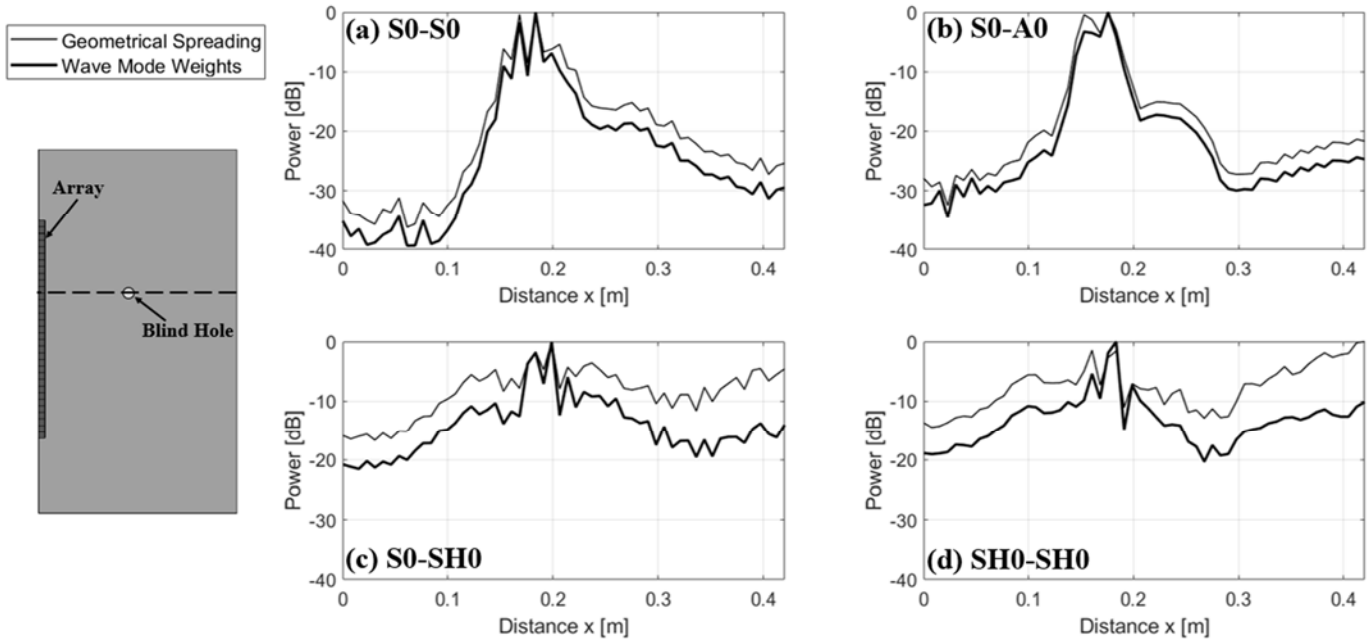

Fig. 12. Line Spread Functions (LSFs) along the x direction for the off-axis blind hole reflector for geometrical spreading only (thin solid line) and wave mode weights (thick solid line). (a) S0-S0 combination. (b) S0-A0 combination. (c) S0-SH0 combination. (d) SH0-SH0 combination. Coordinates of the defect center x=0.19, y=0.30 m.

reduction of artifacts and boundary reflections that can be achieved with the proposed set of wave mode weights. For instance, the values around 0.1m in Fig. 12(d), which are artifacts related to a faster wave mode combination than SH0-SH0, are decreased by 5dB.

The differences between the actual and the detected position of the defect were 0.0067m, 0.0144m, 0.0085m, and 0.0067m along the x direction (axial position) and 0.004m, 0.0029m, 0.0029m, and 0.004m along the y direction (lateral position) for the S0-S0, the S0-A0, the S0-SH0, and the SH0-SH0 combinations, respectively.

The compounding of the different wave mode combinations for the off-axis case is shown in Fig. 13. Incoherent and coherent compounding show, again, a very significant improvement compared to any of the individual mode combinations, with increased dynamic range and spatial resolution. The errors in terms of location of the reflectors were 0.0067m along the x direction (axial position) and 0.004m along the y direction (lateral position) for both incoherent and coherent compounding.

In summary, the location of the reflector in the plate (on-axis or off-axis) does not seem to alter the general improvements obtained in the MVDR images by the wave structure weights and the wave mode compounding.

E. Results: Multiple Reflectors

The last analysis was performed for the case of multiple reflectors on the aluminum plate. Two blind holes placed at x = 0.19m, y = 0.38m and at x = 0.19m, y = 0.42m were considered. The spacing of the holes was 0.04m and their depth was equal to half of the plate thickness. Only the S0-S0 and the S0-A0 wave mode combinations were considered. Figs. 14(a) and (c) show the images obtained for the S0-S0 combination using the MVDR beamformer with geometrical spreading only and with wave mode weights, respectively. Similarly to the case of single reflector, the wave mode weights show an improvement in terms of dynamic range, reducing artifacts and side lobes around the location of the actual reflectors. Figs. 14(b) and (d) show the results for the S0-A0 combination using geometrical spreading only and wave mode weights, respectively. Also in this case, the wave mode weights perform better than the geometrical spreading, showing an increased dynamic range and improved spatial resolution.

Figs. 14(e) and (f) illustrate the Line Spread Functions (LSFs) for the S0-S0 and the S0-A0 combinations, respectively, obtained from the images in Figs. 14(a)-(d). The LSFs are plotted at x = 0.19m (the location of the reflectors). From

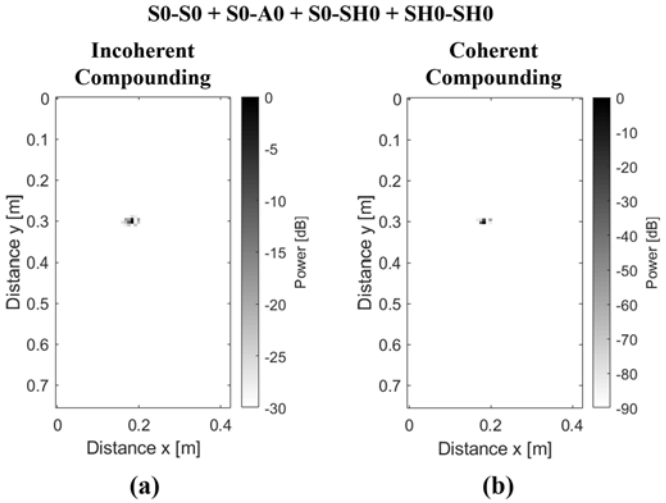

Fig. 13. Results obtained for the off-axis reflector location after compounding the S0-S0, S0-A0, S0-SH0, and SH0-SH0 wave mode combinations (a) incoherently and (b) coherently. Coordinates of the defect center x=0.19, y=0.30 m.

This article has been accepted for publication in a future issue of this journal, but has not been fully edited. Content may change prior to final publication. Citation information: DOI 10.1109/TUFFC.2019.2935139, IEEE Transactions on Ultrasonics, Ferroelectrics, and Frequency Control

Fig.14(e) it is possible to see how the S0-S0 combination with wave mode weights shows an average dynamic range improvement of ~2dB when compared to the geometrical spreading weights. Similarly, the S0-A0 combination (Fig. 14(f)) with wave mode weights also brings an average increase of ~2dB in dynamic range. Additionally, the wave mode weights applied to the S0-A0 combination allow separating the two reflectors until -10.5dB, whereas the geometrical spreading weights can only resolve them until -7.5dB.

The differences between the actual and the detected position of the defects were 0.0067m and 0.0144m along the x direction (axial position) and 0.0015m and 0.0015m along the y direction (lateral position) for the S0-S0 and the S0-A0 combinations, respectively.

Figs. 15(a) and (b) show the results of incoherent and coherent wave mode compounding, respectively, on the plate with two reflectors. Also in this case, only the S0-S0 and the S0-A0 wave mode combinations were considered. The images show that compounding allows removing artifacts and side lobes, compared to the images in Fig. 14, focusing the energy on the correct locations of the two blind holes. Moreover, both compounding techniques show a clear separation of the reflectors, with the coherent compounding performing better than the incoherent version due to the added cross-mode terms. The errors in terms of location of the reflectors were 0.0067m along the x direction (axial position) and 0.0015m along the y direction (lateral position) for both incoherent and coherent compounding.

VI. Discussion and Conclusions

This paper has investigated improvements to the MVDR beamforming imaging algorithm applied to ultrasonic guided waves in plates (Lamb modes). The improvements consist of (a) the use of weights, or MVDR replica vectors, based on the distribution of displacements (mode structure) as received by the transducer array, and (b) the combination, or compounding, of multiple Lamb modes to create an improved image of reflectors (e.g. damage) in the plate.

Closed-form expression for the mode structure weights were derived for reflected symmetric modes S0, antisymmetric modes A0, and shear horizontal modes SH0. Geometrical spreading of the waves in transmission and reception was also included in the analytical formulation of the weights. The application of the weights for the different wave modes was performed in a matched field processing approach. The goal is to match, for every point in the imaging domain, the measured amplitude distribution across the array with the expected amplitude distribution based on the physics of the propagating guided wave modes. The effectiveness of these weights is fully exploited in the case of circular wavefronts, or reflectors close to the array (near field). In the far field of the array, these

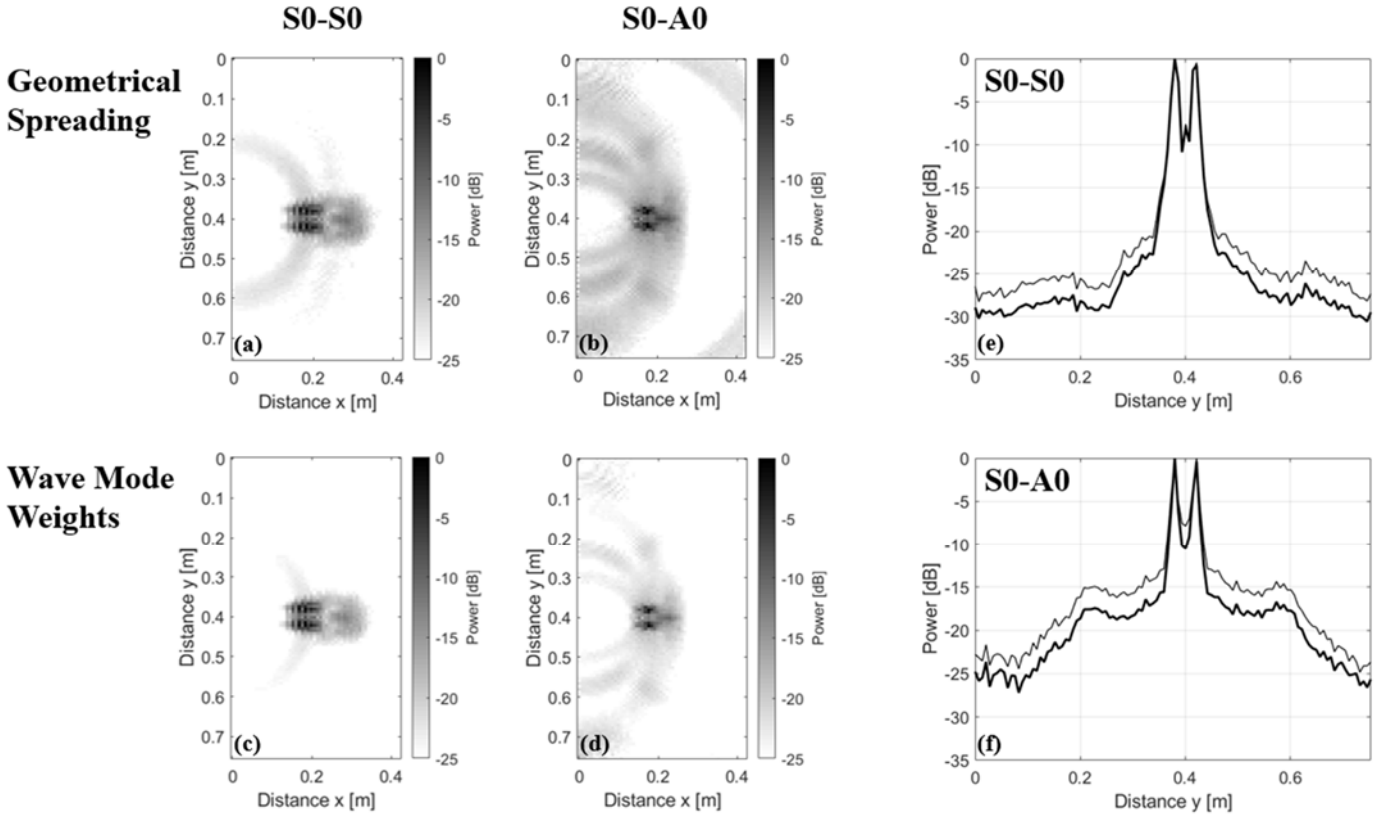

Fig. 14. Numerical results for the plate with multiple damages (two blind holes) obtained using MVDR with geometrical spreading only and wave mode weights. (a) and (b) Results obtained with geometrical spreading for the S0-S0 and S0-A0 combinations, respectively. (c) and (d) Results obtained using wave mode weights for the S0-S0 and S0-A0 combinations, respectively. (e) and (f) Line Spread Functions (LSFs) along the y direction for the S0-S0 and S0-A0 combinations, respectively, using geometrical spreading only (thin solid line) and wave mode weights (thick solid line). Coordinates of the defect centers x=0.19, y=0.30 and y=0.42 m.

This article has been accepted for publication in a future issue of this journal, but has not been fully edited. Content may change prior to final publication. Citation information: DOI 10.1109/TUFFC.2019.2935139, IEEE Transactions on Ultrasonics, Ferroelectrics, and Frequency Control

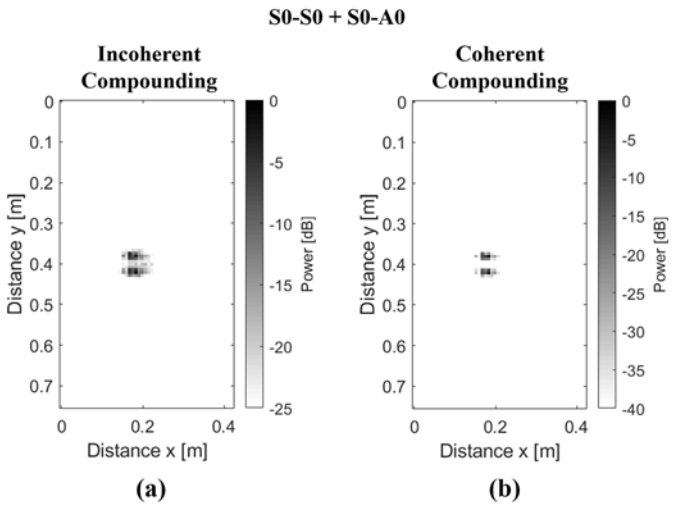

Fig. 15. Results obtained for the plate with two blind holes after compounding the S0-S0 and the S0-A0 wave mode combinations (a) incoherently and (b) coherently. Coordinates of the defect centers x=0.19, y=0.30 and y=0.42 m.

wavefronts will tend to a planar wavefront and thus a constant displacement distribution over the array, for every point in the medium, which does not improve the focus on the damage location.

The paper also exploits the opportunity of compounding different wave mode combinations obtained from multiple guided wave modes naturally existing in the plate, in order to increase the array gain without increasing its physical aperture. The compounding can be performed either coherently or incoherently, in analogy with the combination of multiple excitation events or frequencies.

A proof-of-principle study demonstrating these improvements was performed using an FEM model of an aluminum plate with an antisymmetric reflector (blind hole) located either on-axis or off-axis with respect to the transducer array. Four different wave mode combinations were considered, namely S0-S0, S0-A0, S0-SH0, and SH0-SH0. For both on-axis and off-axis reflector locations, the wave mode weights as well as the wave mode compounding showed substantial increases in dynamic range, decrease in sidelobe levels, and improved spatial resolution as compared to a classical MVDR framework utilizing simple geometrical wave spreading as the replica vectors. The compounding resulted in the most dramatic improvements in image quality compared to the use of individual modes.

These concepts can be extended to more general cases of guided wave propagation than the specific cases examined in the numerical study. For example, results were only shown for the S0 mode and the SH0 mode in transmission. These can be easily extended to the A0 mode in transmission, which would bring additional opportunities for wave mode compounding. In a practical experiment, the choice of the type and the position of the transducer array will largely dictate the specific Lamb modes that can be utilized for imaging. Similarly, the specific mode frequency and plate thickness combination will dictate whether higher-order guided modes can exist and can be used for further image improvements.

The technique requires mode separation, which may be challenging for reflectors located very close to the array. This is a common problem of ultrasonic imaging. One possibility in cases where mode separation may be challenging is to obtain mode compression using chirped excitations.

Dispersion does not negatively affect this analysis because the narrowband signals utilized result in essentially constant velocities for each of the propagating modes.

The results shown in this study were only numerical. While the results from real experimental measurements could be different, the numerical analysis shows the potential advantages obtainable in practice. Experimental studies on these and other types of defects should be carried out in future studies. The practical implementation of these techniques would require an ability to simultaneously detect multiple wave modes. This ability is already present in most piezoelectric transducers used in guided-wave ultrasonic testing. The possibility of using a combination of longitudinal-type piezoelectric transducers (for S0 and A0) and shear-type transducers (for SH0) to exploit the full spectrum of possible modes also exist.

The 30% RMS numerical noise level artificially added to the received waveforms gives some comfort on the appropriateness of the technique in an actual test affected by measurement noise. In any case, the favorable comparison of the wave structure weights and wave compounding over the geometrical spreading weights is expected to hold for any level of signal noise that is common to the two methods.

The study has also considered a small reflector compared to the incident ultrasonic wavelength. The possibility of including specific scattering patterns from reflectors of general size and orientation in the proposed MVDR wave structure weights should also be the focus of a future study.

REFERENCES

[1] G. Montaldo, M. Tanter, J. Bercoff, N. Benech and M. Fink, "Coherent plane-wave compounding for very high frame rate ultrasonography and transient elastography," *IEEE Trans. Ultrason. Ferroelectr. Freq. Control*, Vol. 56, no. 3, pp. 489-506, 2009.

[2] C. Papadacci, M. Pernot, M. Couade, M. Fink and M. Tanter, "High-contrast ultrafast imaging of the heart," *IEEE Trans. Ultrason. Ferroelectr. Freq. Control*, Vol. 61, no. 2, pp. 288-301, 2014.

[3] M. Tanter and M. Fink, "Ultrafast imaging in biomedical ultrasound," *IEEE Trans. Ultrason. Ferroelectr. Freq. Control*, Vol. 61, no. 1, pp. 102-119, 2014.

[4] M. F. Rasmussen and J. A. Jensen, "Comparison of 3-D synthetic aperture phased-array ultrasound imaging and parallel beamforming," *IEEE Trans. Ultrason. Ferroelectr. Freq. Control*, Vol. 61, no. 10, pp. 1638-1650, 2014.

[5] M. Karaman, P. C. Li and M. O'Donnell, "Synthetic aperture imaging for small scale systems," *IEEE Trans. Ultrason. Ferroelectr. Freq. Control*, Vol. 42, no. 3, pp. 429-442, 1995.

[6] C. H. Frazier and W. D. O'Brien, "Synthetic aperture techniques with a virtual source element," *IEEE Trans. Ultrason. Ferroelectr. Freq. Control*, Vol. 45, no. 1, pp. 196-207, 1998.

[7] G. R. Lockwood, J. R. Talman and S. S. Brunke, "Real-time 3D ultrasound imaging using sparse synthetic aperture beamforming," *IEEE Trans. Ultrason. Ferroelectr. Freq. Control*, Vol. 45, no. 4, pp. 980-988, 1998.

[8] C. R. Hazard and G. R. Lockwood, "Theoretical assessment of a synthetic aperture beamformer for rail-time 3-D imaging," *IEEE Trans. Ultrason. Ferroelectr. Freq. Control*, Vol. 46, no. 4, pp. 972-980, 1999.

[9] S. I. Nikolov and J. A. Jensen, "In-vivo synthetic aperture flow imaging in medical ultrasound," *IEEE Trans. Ultrason. Ferroelectr. Freq. Control*, Vol. 50, no. 7, pp. 848-856, 2003.

[10] J. A. Jensen, S. I. Nikolov, K. L. Gammelmark, and M. H. Pedersen, "Synthetic aperture ultrasound imaging," *Ultrasonics*, Vol. 44, Suppl. 1, pp. e5-e15, 2006.

[11] N. Oddershede and J. A. Jensen, "Effects influencing focusing in synthetic aperture vector flow imaging," *IEEE Trans. Ultrason. Ferroelectr. Freq. Control*, Vol. 54, no. 7, pp. 1811-1825, 2007.

[12] P.D. Wilcox, "Omni-directional guided wave transducer arrays for the rapid inspection of large areas of plate structures," *IEEE Trans. Ultrason. Ferroelectr. Freq. Control*, Vol. 50, no. 6, pp. 699-709, 2003.

[13] C. H. Wang, J. T. Rose and F-K. Chang, "A synthetic time-reversal imaging method for structural health monitoring," *Smart Mater. Struct.,* vol. 13, no. 2, pp. 415-423, 2004.

[14] A. S. Purekar, D. J. Pines, S. Sundararaman and D.E. Adams, "Directional piezoelectric phased array filters for detecting damage in isotropic plates," *Smart Mater. Struct*., vol. 13, no. 4, pp. 838–850, 2004.

[15] L. Yu and V. Giurgiutiu, "In situ 2-D piezoelectric wafer active sensors array for guided wave damage detection," *Ultrasonics*, vol. 48, no. 2, pp. 117–134, 2008.

[16] L. Ambrozinski. *Beamforming of guided waves*. Chapter 7 of *Advanced Structural Damage Detection: From Theory to Engineering Applications*, T. Stepinski, T. Uhl and W. Staszewski eds., pp. 177-211, John Wiley and Sons, Ltd., 2013.

[17] T. Clarke, P. Cawley, P. D. Wilcox and A. J. Croxford, "Evaluation of the damage detection capability of a sparse-array guided-wave SHM system applied to a complex structure under varying thermal conditions," *IEEE Trans. Ultrason. Ferroelectr. Freq. Control*, Vol. 56, no. 12, pp. 2666–2678, 2009.

[18] J. S. Hall and J. E. Michaels, "Minimum variance ultrasonic imaging applied to an in situ sparse guided wave array," *IEEE Trans. Ultrason. Ferroelectr. Freq. Control*, Vol. 57, no. 10, pp. 2311–2323, 2010.

[19] J. S. Hall and J. E. Michaels, "Multipath ultrasonic guided wave imaging in complex structures," *Struct. Health Monit.*, vol. 14, no. 4, pp. 345-358, 2015.

[20] E. B. Flynn, M. D. Todd, P. D. Wilcox, B. W. Drinkwater and A. J. Croxford, "Maximum-likelihood estimation of damage location in guided-wave structural health monitoring," *Proc. Roy. Soc. A: Math. Phy.*, vol. 471, no. 2181, pp. 2575–2596, 2011.

[21] J. B. Harley and J. M. F. Moura, "Data-driven matched field processing for Lamb wave structural health monitoring," *J. Acoust. Soc. Am.*, vol. 135, no. 3, pp. 1231–1244, 2014.

[22] M. Engholm and T. Stepinski, "Adaptive beamforming for array imaging of plate structures using Lamb waves," *IEEE Trans. Ultrason. Ferroelectr. Freq. Control*, Vol. 57, no. 12, pp. 2712–2724, 2010.

[23] J. Zhang, B. W. Drinkwater and P. D. Wilcox, "Defect characterization using an ultrasonic array to measure the scattering coefficient matrix," *IEEE Trans. Ultrason. Ferroelectr. Freq. Control*, vol. 55, no. 10, pp. 2254-2265, 2008.

[24] J. S. Hall, P. Fromme and J. E. Michaels, "Guided wave damage characterization via minimum variance imaging with a distributed array of ultrasonic sensors," *J. Nondestr. Eval.*, vol. 33, no. 3, pp. 299-308, 2014.

[25] F. Lanza Di Scalea, S. Sternini, and T. V. Nguyen, "Ultrasonic imaging in solids using wave mode beamforming," *IEEE Trans. Ultrason. Ferroelectr. Freq. Control*, vol. 64, no. 3, pp. 602–616, 2017.

[26] S. Sternini, A. Quattrocchi, R. Montanini, A. Pau and F. Lanza di Scalea, "A match coefficient approach for damage imaging in structural components by ultrasonic synthetic aperture focus," *Proc. Eng.*, vol. 199, pp. 1544-1549, 2017.

[27] R. Sicard, J. Goyette and D. Zellouf, "A SAFT algorithm for lamb wave imaging of isotropic plate-like structures," *Ultrasonics*, vol. 39, no. 7, pp. 487-494, 2002.

[28] R. Sicard, A. Chahbaz and J. Goyette, "Guided Lamb waves and L-SAFT processing technique for enhanced detection and imaging of corrosion defects in plates with small depth-to-wavelength ratio," *IEEE Trans. Ultrason. Ferroelectr. Freq. Control*, vol. 51, no. 10, pp. 1287-1297, 2004.

[29] J. Davies, F. Simonetti, M. Lowe, P. Cawley, "Review of synthetically focused guided wave imaging techniques with application to defect sizing," in *Review of Progress in Quantitative NDE*, vol. 25, ed. by D. O. Thompson, D. E. Chimenti (American Institute of Physics, Melville, New York), 2006, pp. 142-149.

[30] A.B. Baggeroer, W. A. Kuperman and P. N. Mikhalevsky, "An overview of matched field methods in ocean acoustics," *IEEE Ocean. Eng.*, vol. 18, no. 4, pp. 401-424, 1993.

[31] W. A. Kuperman and G. Turek, "Matched field acoustics," *Mech. Syst. Sig. Proc.*, vol. 11, no. 1, pp. 141-148. 1997.

[32] J. Capon, "High resolution frequency wavenumber spectrum analysis," *Proc. IEEE*, vol. 57, pp. 1408-1418, 1969.

[33] F. Arabshahi, S. Monajemi, H. Sheikhzadeh, K. Raahemifar and R. Faraji-Dana, "A frequency domain MVDR beamformer for UWB microwave breast cancer imaging in dispersive mediums," *IEEE International Symposium on Signal Processing and Information Technology*, Athens, 2013, pp. 000362-000367.

[34] J. F. Synnevag, A. Austeng and S. Holm, "Adaptive beamforming applied to medical ultrasound imaging," *IEEE Trans. Ultrason. Ferroelectr. Freq. Control*, vol. 54, no. 8, pp. 1606-1613, 2007.

[35] A. M. Deylami, J. A. Jensen and B. M. Asl, "An improved minimum variance beamforming applied to plane-wave imaging in medical ultrasound," *2016 IEEE International Ultrasonics Symposium (IUS)*, Tours, 2016, pp. 1-4.

[36] K. Diamantis, A. Greenaway, T. Anderson, J. A. Jensen and V. Sboros, "Experimental performance assessment of the sub-band minimum variance beamformer for ultrasound imaging," *Ultrasonics*, vol. 79, pp. 87-95, 2017.

[37] A.B. Baggeroer, W. A. Kuperman, and H. Schmidt, "Matched-field processing: source localization in correlated noise as an optimum parameter estimation process," *J. Acoust. Soc. Am.*, vol. 83, pp. 571-587, 1988.

[38] Z-H. Michalopoulou and M. B. Porter, "Matched-field processing for broad-band source localization," *IEEE Ocean. Eng.*, vol. 21, no. 4, pp. 384-392, 1996.

[39] N.C. Makris, "A foundation for logarithmic measures of fluctuating intensity in pattern recognition," *Opt. Lett*., vol. 20, pp. 2012-2014, 1995.

[40] C. Debever and W. A. Kuperman, "Robust matched-field processing using a coherent broadband white noise constraint processor," *J. Acoust. Soc. Am.*, vol. 122, no. 4, pp. 1979-1986, 2007.

[41] A. Tolstoy, *Matched Field Processing*, World Scientific, New York, 1993.

[42] G. J. Orris, M. Nicholas, and J. S. Perkins, "The matched-phase coherent multi-frequency matched-field processor," *J. Acoust. Soc. Am.*, vol. 107, no. 5, pp. 2563-2575, 2000.

[43] F. B. Jensen, W. A. Kuperman, M. B. Porter and H. Schmidt, "Signals in noise," in *Computational Ocean Acoustics,* 2nd ed., Springer Publishing Company, Inc., 2011, pp. 705-772.

[44] A. Pau and D. V. Achillopoulou, "Interaction of shear and Rayleigh-Lamb waves with notches and voids in plate waveguides," *Materials*, vol. 10, no. 7, 841, 2017.

[45] J. L. Rose, "Waves in plates," in *Ultrasonic Guided Waves in Solid Media*, Cambridge University Press, 2014, pp. 76-106.

[46] O. Diligent, "Interaction between fundamental Lamb modes and defects in a plate", PhD Thesis, 2003, pp. 57-62.

[47] B. R. Mace and E. Manconi, "Modelling wave propagation in two-dimensional structures using finite element analysis," *J. Sound Vib.*, vol. 318, no. 4-5, pp. 884-902, 2008.